FLOW Lab

Preprint version of the article submitted to the Journal of Aircraft in Feb 2025.
The content of this paper may differ from the final publisher version.

Mission-Focused Multidisciplinary Design Optimization of Tilt-Rotor eVTOL Propulsion System

Tyler Critchfield* and Andrew Ning†
Brigham Young University, Provo, Utah, 84602

Tilt-rotor propulsion system design requires a multidisciplinary approach to tackle important challenges and competing tradeoffs between disciplines. In this paper, we model rotor aerodynamics, blade structures, vehicle drag, electric propulsion, and tonal/broadband acoustics for a tilt-rotor, electric vertical takeoff and landing aircraft using low-to-mid fidelity tools. We use gradient-based design optimization with automatic differentiation and parameter sensitivity analyses to explore the design space and complex tradeoffs of tilt-rotor distributed electric propulsion systems, exploring effects of variations in payload/empty weight, battery specific energy, and blade tip speed. This framework models multiple operating points with a mission-focused objective to account for the effects of both hover and cruise conditions on the overall system performance. Additionally, we develop a Pareto front between range and noise and observe that, for the same noise output, modeling tonal and broadband noise increases range by 3.1% when compared to using a Mach tip speed surrogate acoustics model.

Nomenclature

c	=	chord (m)
C_{D_P}	=	parasitic drag coefficient
c_d	=	2D drag coefficient
c_l	=	2D lift coefficient
$C_{T,\text{hover}}$	=	thrust coefficient in hover, $T/(\rho\pi\Omega^2 R_{\text{tip}}^3)$
$C_{T,\text{cruise}}$	=	thrust coefficient in cruise, $4\pi^2 T/(\rho\Omega^2 R_{\text{tip}}^4)$
D	=	total drag (N)
K_v	=	motor constant (rad/s/V)
L	=	lift (N)
m	=	mass (kg)
OCV	=	battery open current voltage (V)
r	=	radial location along the blade (m)
R_{tip}	=	blade radius (m)
SOC	=	battery state of charge
T	=	Thrust (N)
t_{ply}	=	ply thickness (mm)
V_∞	=	cruise velocity (m/s)
η_{prop}	=	propulsive efficiency
Ω	=	rotational speed (rad/s)
ρ	=	density (kg/m^3)

I. Introduction

Urban air mobility (UAM) is an emerging industry that has the potential to revolutionize modern transportation systems. UAM presents a challenging problem that requires careful study from multiple disciplines to design aircraft that are safe, quiet, and economically viable. A subset of UAM designs are electric vertical takeoff and landing

*Doctoral Candidate, Mechanical Engineering, AIAA Student Member; trcritchfield@gmail.com (Corresponding Author).
†Associate Professor, Mechanical Engineering, AIAA Associate Fellow

(eVTOL) aircraft , which can operate effectively in dense, urban areas with low environmental emissions and without the need for a traditional runway. NASA researchers have introduced several conceptual design configurations for eVTOL aircraft, including single- and multi-rotor helicopters and designs that obtain cruise lift from wing lifting surfaces such as the tilt-rotor, tilt-wing, and lift+cruise concepts [1–5].

In this study we limit our scope to modeling tilt-rotor configurations, where rotors provide vertical lift to the aircraft during hover, climb, and landing phases, and the same rotors then rotate to provide horizontal thrust in cruise while the wing provides lift. (See Fig. 1 for an example of a tilt-rotor configuration from Joby). Like any eVTOL configuration, there are benefits and costs to such a design. For instance, lift generated from a wing rather than rotors is more energy efficient [6, 7]; however, there is also increased mechanical and control complexity to rotate rotors mid-flight with collective pitch. Despite potential weight benefits, dual-purpose rotors must involve a compromised design compared to rotors optimized for a single stage of flight. The aim of this paper is to understand this tradeoff between hover and cruise performance for the same rotors.

Fig. 1 Joby S-4 pre-production prototype tilt-rotor aircraft. Credit: Vertical Flight Society

Gradient-based design optimization is an important tool to understand these complex and relatively new design spaces. Gradient-based methods also have the advantage of scaling well with increasing numbers of design variables, but require smooth and accurate derivative computation. Algorithmic differentiation (AD) methods are critical to provide adequate scaling and accuracy (as opposed to finite difference methods, for example). Several studies have used optimization to model UAM propellers and propeller systems [8–10]; often these works focus only on aerodynamic modeling and performance, which can neglect other important design factors that need to be considered. Incorporating several disciplines in a multidisciplinary design optimization (MDO) yields insights on tradeoffs between different aircraft systems. There are plenty of examples of using MDO in the literature to design eVTOL propulsion systems, with varying combinations of disciplines modeled. For instance, several works have combined aerodynamic and power train or flight dynamics models in an MDO frameowrk, including Hendricks et al. [11, 12], Hoyos et al. [13], Mian et al. [14], and Xia et al. [15]. Other researchers have performed aeroacoustic design optimizations of propellers, including Zawodney et al. [16], Gur et al. [17], and Ingraham et al. [18], though these works focus only on hover conditions.

Other researchers have used MDO to study propulsion systems with more than two disciplines. Moore and Ning [19] and Hwang and Ning [20] used gradient-based MDO to design propellers for the NASA X-57 short-takeoff and landing (STOL) aircraft concept. Moore was able to reduce the X-57 takeoff distance by 43% compared to a baseline design considering propeller and wing aerodynamics, structures, power train, and acoustics. Hwang used MDO to increase the X-57 range by 12%, while considering propeller and wing aerodynamics, flight dynamics, structures, and propulsion models (though acoustics were not considered). Shahjahan et al. [21] applied gradient-free MDO to the UAM tilt-rotor application, combining models for aerodynamics, structures, and acoustics to look at hover, cruise, and transition operating points. They found that including transition increases the required hover power by about 5%.

These works and others have leveraged MDO to make powerful steps forward in our understanding of eVTOL propulsion system design. However, there is more to learn. Many of these studies only focus on one or two disciplines; those that include more have their own limitations, such as using gradient-free methods (which are limited in the number of design variables that can be optimized), focusing only on one operating condition (often hover), or neglecting a mission-focused objective. The latter is especially key for tilt-rotor systems. Rotors that are engineered to perform well in both hover and cruise need high-level mission analysis or the final design will become an arbitrarily weighted average of the optimal designs of the operating points. A mission-based objective helps solve this problem (e.g., by optimizing range or endurance rather than aerodynamic efficiency).

In this paper, we apply gradient-based MDO to a fully-electric tilt-rotor eVTOL propulsion system. Our MDO framework includes blade geometry design and focuses on mission-level performance tradeoffs for propulsion systems that must operate effectively in hover and cruise conditions. We model propeller aerodynamics, blade structures, vehicle drag, electric propulsion, and rotor acoustics using low- and mid-fidelity methods. This is the first study that includes such disciplines in a gradient-based, mission-focused MDO framework for a tilt-rotor application. We place an emphasis on parameter sensitivity analysis, seeking to understand how variations in vehicle weight, blade tip speed, battery specific energy, and rotor blade count affect mission-level performance and optimal blade geometries. These results lend further insight to the unique tradeoffs between hover and cruise performance for tilt-rotor systems. We also explore the effects of explicitly modeling tonal and broadband acoustics and compare these results to those that use a blade tip speed constraint as a surrogate acoustics model.

II. Methods

In this section, we describe the mission profile, optimization approach, and analysis models used in this work. Our main focus is propeller optimization, so we use medium-fidelity models for propeller aerodynamics (blade element momentum theory), blade structures (geometrically exact beam theory with composite layup mesh), and tonal acoustics (Ffowks-Williams Hawkings equations). We include lower-fidelity models for broadband noise, electric propulsion, aircraft drag, and mission profile.

A. Propeller aerodynamics

The propeller aerodynamics are modeled using blade element momentum theory (BEMT), which has been used extensively in propeller analysis [11–13, 18–20, 22]. BEMT combines a momentum balance and airfoil analysis along the rotor blade, integrating discretized outputs to yield a total thrust, torque, and loading distribution along the blade. Using the method developed by Ning [23, 24], a solution can be found from combining these two analyses that is continuous and guaranteed to converge, making it ideal for design optimization. We use the implementation in CCBlade.jl [24], which is able to calculate exact derivatives using AD methods. CCBlade is able to compute derivatives efficiently without needing to pass them through every iteration of its internal solver using an implicit formulation [25].

We supply the BEMT model with precomputed polars, described in Section II.B. We apply precomputed rotational corrections (Du Selig for lift [26] and Eggers for drag [27]) to the polars based on blade properties at 75% of the blade radius and extrapolate the data to high angles of attack using the Viterna method [28]. In the BEMT model, we employ hub and tip loss corrections from Prandtl [29] and include a correction for the induction factor from Buhl [30] that is a modification of Glauert's method [31]. Additionally, we assume steady inflow conditions and neglect interactions between blade sections, between adjacent rotor wakes, and between rotor wakes and vehicle surfaces.

B. Airfoil aerodynamics

The thickness of each blade element airfoil section is a crucial design parameter for the optimizer to strengthen the blade. However, this thickness also affects aerodynamic performance. While airfoil shape design is not the focus of this work, we could not neglect the aerodynamic effects of changing airfoil thickness. The extreme needs of tilt-rotor propulsive systems (especially in the hover operating condition when the propellers need to support the entire aircraft weight) make the use of an off-the-shelf family of airfoils (e.g., NACA 44-series) prohibitive; they cannot provide adequate lift with the power constraints of the battery.

To meet this need for thickness variation with high-performaning polars, we generated a series of airfoil geometries based on the MH-114 airfoil, ranging in maximum thickness-to-chord (t/c) ratio from 6% to 24% while preserving the camber and relative thickness distribution of the MH-114 airfoil. We fit these geometries using the CST parameterization [32] to ensure a rounded leading edge (see Fig. 2). We generated polar data for each airfoil using XFOIL [33] at a constant Reynolds number of 1×10^6 and Mach numbers ranging from 0 to 0.7.

After running the airfoils in Fig. 2 through XFOIL, we fit the space to a 3D B-spline, with inputs consisting of angle of attack, airfoil t/c ratio, and Mach number. A subset of this contour space is shown in Fig. 3 (where the fixed values for Mach number and t/c ratio correspond approximately to the blade section at 75% of the blade radius). With this 3D polar space, the optimizer uses the airfoil thickness distribution along the rotor blade as design variables, and the resulting outputs and derivatives are smooth and continuous.

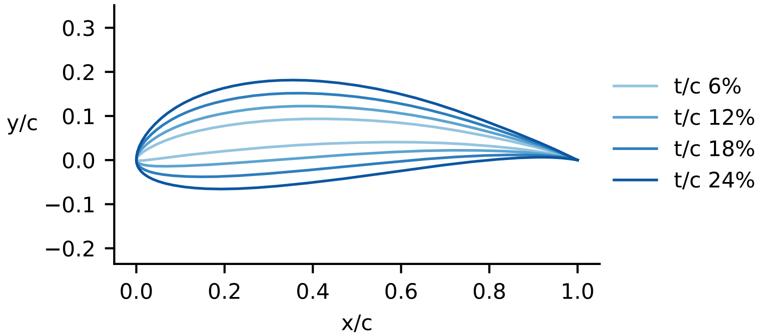

Fig. 2 Airfoil geometries with maximum t/c ratios spanning from 6% to 24%.

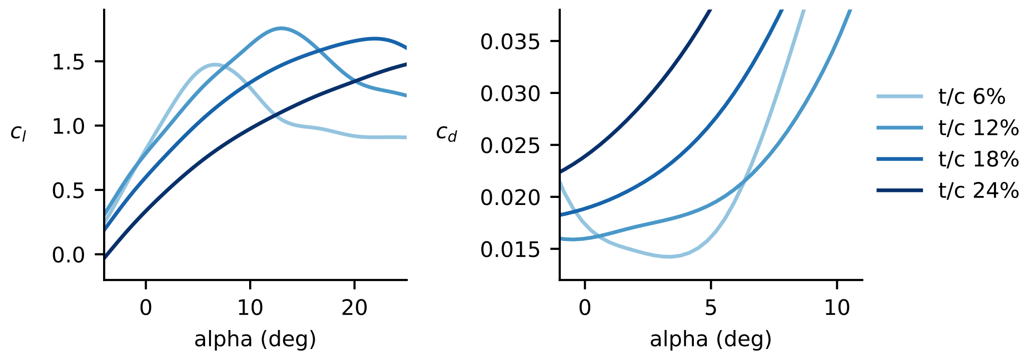

(a) Lift and drag coefficients with varying t/c ratios from 6–24% at Mach 0.378.

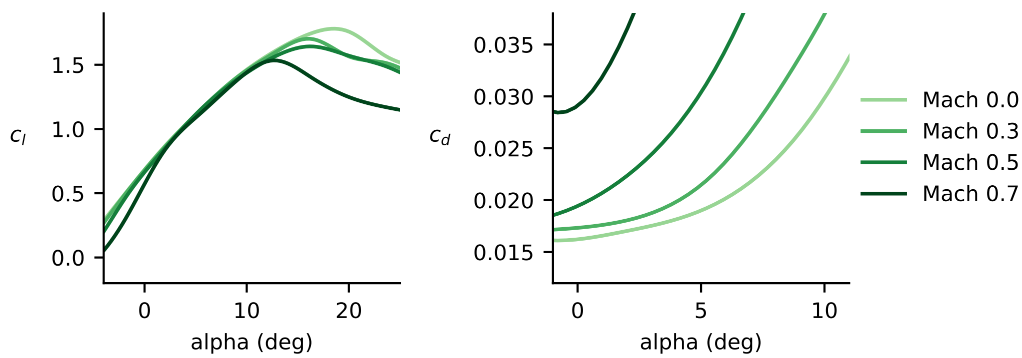

(b) Lift and drag coefficients with varying Mach numbers from 0.0–0.7 at a t/c ratio of 0.158.

Fig. 3 A subset of 2D airfoil polars used in this study.

C. Blade structures

We model the rotor blade as a cantilever beam with geometrically exact beam theory [34, 35]. We use one-way coupling to couple this beam model to the aerodynamic BEMT solution (i.e., loads from the BEMT solution are passed to the beam analysis; deflections from the beam analysis are not accounted for in the BEMT analysis). We model the cross-section as a shell composite layup of high modulus carbon fiber reinforced polymer (CFRP) material. CFRP properties are listed in Tables 1 and 2, where x_t, y_t, x_c, y_c, and s refer to the first and second axis failure strengths in tension, first and second axis failure strengths in compression, and the shear failure strength, respectively. In the shell layup, unidirectional CFRP tape runs along the blade span to increase bending stiffness; bidirectional CFRP weave oriented at 45° is placed on either side of the tape for torsional rigidity. In the optimization, we fix the orientations and thicknesses of the weave layers and allow the optimizer to change the tape thickness at every blade section.

Table 1 CFRP Material Stiffness Properties

Material	E_1 (GPa)	E_2 (GPa)	G_{12} (GPa)	ν_{12}	ρ (kg/m^2)	t_{ply} (mm)
CFRP Tape	175.0	8.0	5.0	0.3	1,600.0	0.152
CFRP Fabric	85.0	85.0	5.0	0.1	1,600.0	0.218

Table 2 CFRP Material Strength Properties

Material	x_t (MPa)	y_t (MPa)	x_c (MPa)	y_c (MPa)	s (MPa)
CFRP Tape	806.0	671.9	29.62	166.7	53.57
CFRP Fabric	282.1	118.6	259.2	125.0	31.25

We calculate cross-sectional stiffness properties using a finite element mesh that uses the entire 6x6 Timoshenko stiffness matrix (see Fig. 4). We then calculate strain recovery using the mesh and beam analysis results and determine failure based on the Tsai Wu criterion [36]. These methods are implemented in GXBeam [37], a Julia package that allows for exact derivative calculation through the entire process. Recreating the mesh at every iteration is inefficient and prone to discontinuity. To make the meshing process suitable for optimization, we use a mesh-morphing procedure that alters the existing mesh based on new chord and thickness values. The mass of each blade section is integrated to get the blade mass, which is multiplied by the number of blades (along with a 10% mass markup for the hub) to get rotor mass. The mass of all rotors in the system is added to the total system mass.

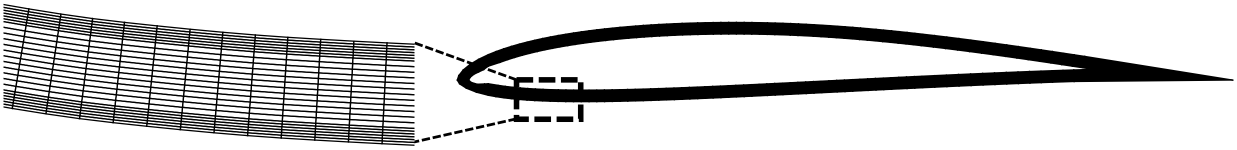

Fig. 4 Finite element mesh of an example shell layup.

D. Acoustics

We use two approaches to model noise in this paper. The first, used in the aerostructural optimizations, uses a Mach tip speed constraint as a surrogate noise model. The second, used in the aero-structural-acoustic optimizations, models tonal and broadband noise directly. We model tonal noise using AcousticAnalogies.jl*, a pure-Julia implementation of the Ffowks-Williams Hawkings (FWH) equations [38]. This implementation uses the compact form [39] of Farassat's F1A formulation [40]. AcousticAnalogies models the monopole (thickness) and dipole (loading) noise sources using rotor geometry, rotational velocity, and blade loading inputs, and neglects quadrupole noise sources.

We model broadband noise sound pressure level using an empirical model developed by Gill and Lee [41]:

$$SPL_{1/3} = \frac{f_1 \Delta^{0.6}}{(\Delta + f_2)^{f_3} + (C_T \Delta)^{f_4}} \tag{1}$$

*developed by Daniel Ingraham at NASA Glenn Research Center: https://github.com/OpenMDAO/AcousticAnalogies.jl where $\Delta = S_t - \left(\sigma \log_{10} C_T + f_5 \log_{10} \sigma\right)$. $S_t = fc/V_\infty$ is the Strouhal number based on the solidity-weighted chord length ($c = \sigma\pi R_{\text{tip}}/B$), σ is the rotor solidity and B is the number of blades. The terms f_1 to f_5 depend on blade tip speed, V_t (or M_t for tip Mach number), thrust coefficient C_T, distance to the observer from the rotor hub, s_0, and elevation angle of the observer, θ_0:

$$
\begin{aligned}
f_1 &= 10 \log_{10}\left(V_t^{7.84}\right) \\
f_2 &= -2M_t^2 + 2.06 \\
f_3 &= -C_T M_t \left(C_T - \sin|\theta_0| + 2.06\right) + 1 \\
f_4 &= 4.97 C_T \sin|\theta_0| \left(1.5 M_t \left(\frac{s_0}{R_{\text{tip}}}\right) - \left(\frac{s_0}{R_{\text{tip}}}\right) + 15\right) \\
f_5 &= 0.9 M_t \sigma (M_t + 3.82)
\end{aligned}
\tag{2}
$$

The elevation angle is measured from the rotor plane, with positive orientation below the rotor (e.g., 90 deg is directly underneath in the rotor axis). The authors show this model to be of similar accuracy to the popular Brooks, Pope, and Marcolini (BPM) semi-empirical rotor broadband model [42], without requiring boundary layer information.

These models estimate the overall sound pressure level (OASPL), a scalar metric representing the noise output across all frequencies in decibels. The isolated rotor OASPL from both tonal and broadband models can be found separately and then added together using the following equation:

$$
\text{OASPL}_{\text{total}} = 10 \log\left(\sum_i 10^{\text{OASPL}_i/10}\right) \tag{3}
$$

where there are two entities to be summed: tonal OASPL and broadband OASPL. We then apply Eq. (3) to sum OASPL across all rotors in the system. A-weighting is applied to these results to appropriately weight frequencies based on loudness perception experienced by the human ear. We refer to the A-weighted OASPL as A-OASPL with units of dBA.[†] By treating the entire acoustic output as the sum of individual acoustic footprints of the rotors, we are neglecting noise from rotor-on-rotor and rotor-on-wing interactions. We also neglect motor noise and noise from unsteady loading and blade vortex interactions. Tonal A-OASPL in the rotor axis is severely underpredicted when ignoring acoustic effects from unsteady blade loading [43]. Thus, we measure noise in the hover mission segment using a stationary observer 250 ft below the rotor at an angle 45-deg offset from the rotor axis.

E. Propulsion System

The electric propulsion model combines the propeller model from Section II.A with basic motor and battery models. We use a steady-state motor model to compute the input power to the motor shaft, P_b (power output of the battery):

$$
\begin{aligned}
P_b &= i_m v_m \\
i_m &= Q K_v + i_0 \\
v_m &= I_m R_m + \frac{\Omega}{K_v}
\end{aligned}
\tag{4}
$$

where i_m is the motor current, v_m is the motor voltage supplied from the battery (via the motor controller), Q is the required torque (from the BEMT model), K_v is the motor constant, i_0 is the no-load current, and R_m is the motor internal resistance. This model was also used by Gur [17] for propeller optimization. All motors are assumed to be identical and in parallel, with their own speed controllers, all powered by one battery for the aircraft. We set the motor constant K_v as a design variable in the optimization framework. Motor resistance, no-load current, and mass are computed based on the following regressions taken from Bershadsky et al. [44]:

$$
R_m = 0.2092 K_v^{-1.2425} \tag{5}
$$

$$
i_0 = \frac{0.4}{R_m^{0.6}} \tag{6}
$$

$$
\text{mass} = 10^{4.05} \left(K_v\right)^{-0.5329} \tag{7}
$$

[†]For all instances in this paper, dB and dBA units have a reference of 20 μPa.

Battery parameters are based on the Panasonic NCR18650G cell, which has been used in previous studies for eVTOL applications [45]. Both the internal resistance (R_b) and the open current voltage (OCV) are functions of the battery state of charge (SOC); for this battery, a data fit was provided by Zou et al. [46] (although we refit the OCV as a quadratic, rather than sixth-order polynomial for simplicity):

$$\mathrm{OCV(SOC)} = 0.39\ \mathrm{SOC}^2 + 0.07\ \mathrm{SOC} + 3.7 \tag{8}$$

$$R_b(\mathrm{SOC}) = 0.015\ \mathrm{SOC}^2 - 0.025\ \mathrm{SOC} + 0.104 \tag{9}$$

This battery cell has a capacity of 3.55 Ah and a mass of 48 g. This leads to specific energies of 270 Wh/kg and 225 Wh/kg at the cell and pack level, respectively. We adjust the cell mass to reflect a cell-level specific energy of 400 Wh/kg that is more reflective of current/near-future technology [47]; this reflects a pack level specific energy of 333 Wh/kg. We apply an additional 20% markup on the battery mass to account for wiring, the battery management system, and other overhead required in the pack beyond just the cells. The battery pack is made of a number of cells arranged in various modules and submodules. For our purposes, the details of the arrangement are not essential, but we do need to know the total number of cells in series and the total number of cells in parallel; these are design variables in the optimization framework. We also constrain the battery power margin to be positive (i.e., the total requested power does not exceed the maximum power available from the battery).

After each mission segment that occurs over some time interval t, we update the state of charge (SOC) with the following model:

$$\mathrm{SOC}_f = \mathrm{SOC}_i + \frac{t}{2R_bC_b}\left(\mathrm{OCV} - \sqrt{\mathrm{OCV}^2 - 4R_bP_b}\right) \tag{10}$$

where SOC_i and SOC_f represent the initial and final states of charge for a mission segment, P_b comes from Eq. (4), and C_b is the battery capacity. To avoid premature battery degradation, we begin the mission with an SOC of 0.9 and finish with an SOC of 0.2. Our mission uses all of this state of charge; while this cannot represent all mission types (such as those that have shorter missions and/or more frequent rechargings), this represents missions with high energy requirements.

In the vertical climb, vertical descent, and reserve segments, battery properties are obtained from the initial state of charge of each respective segment. For the vertical climb segment, these properties are used with the known time to determine SOC_f using Eq. (10). For the reserve and vertical descent segments, we assume a SOC_f of 0.2 and use Brent's method [48] to work backward and solve for SOC_i of each segment. Then, having solved for the beginning and ending SOC of the cruise stage, we can solve for the unknown cruise endurance t; however, because there is considerable change in SOC during the cruise mission segment, we use OCV and R_b values at the average SOC of the segment. The cruise endurance is then used to solve for range, as explained in Section II.G. The motor and battery masses are added to the total system mass.

F. Aircraft Drag

We use the following model for total drag of the aircraft, which combines parasitic and induced drag:

$$D = C_{D_P} q S_{wet} + \frac{L^2}{q_\infty \pi b^2 e} \tag{11}$$

where q_∞ is the dynamic pressure, b is the wing span, and e is the Oswald efficiency factor. Our estimated values for C_{D_P} and e are 0.033 and 0.66, respectively. These values come from wing parameters listed in Table 3 and by estimating the skin friction coefficient using an empirical fit from Schlichting for turbulent boundary layers [49]. We also include a 10% drag markup to account for wake mixing and other effects not captured by this low-fidelity analysis.

G. Mission Profile

We optimize electric propulsion systems for a tilt-rotor vehicle configuration with parameters listed in Table 3. The propulsion system is modeled under vertical flight and cruise conditions in four stages: vertical climb, cruise, vertical descent, and cruise reserve. The vertical descent portion is not explicitly modeled in this framework; for simplicity, it is assumed to have the same aerodynamic loading and energy requirements as the vertical climb stage. We focus on mission-level performance and neglect controller optimization in our work, so transition flight is neglected. The ascent/descent velocities are fixed at 5 m/s, corresponding to about two minutes of operation in each phase to ascend to and descend from a cruise altitude of 610 m (2,000 ft). The descent segment is followed by a cruise reserve segment the system is required to complete at the end of its battery life that consists of traveling an additional six miles in cruise conditions, per standards from an Uber Elevate 2018 report [50]. Time in the primary cruise segment is determined by the available energy of the battery, after having accounted for expended energy in the ascent, descent, and reserve stages.

Table 3 Parameters used for the tilt-rotor aircraft configuration in this study.

Parameter	Value
# rotors	12
# blades per rotor	6
vehicle weight	3,300 lbs
wing span	14 m
wing area	12 m^2

Rotor and blade geometries remain fixed for the entire mission while we allow different rotor rotational speeds in the vertical and cruise flight segments. We also include a collective pitch in cruise to adapt for higher cruising velocities. In addition, we analyze each design using a one-engine-inoperable (OEI) operating point so the system is able to handle the necessary thrust and power requirements when one of the motors is non-functioning. (In this scenario, we neglect asymmetric loading caused by such an event.) This operating point is assessed in hover mode at the end of the reserve stage when the battery will have the least amount of power and energy to supply to the propulsion system. We give the optimizer the flexibility to change the rotor collective pitch and rotational speed for this operating condition, though the rest of the design remains unchanged. While the OEI operating point informs many of the optimization constraints, the objective is determined from normal operating conditions.

We determine range using the following expression:

$$\text{Range} = \frac{P_{b,c} t_c \eta}{D} \tag{12}$$

where D is the total vehicle drag, η is the product of the motor and propeller efficiencies, and $P_{b,c}$ and t_c are the battery output power and time duration in the cruise phase, respectively. In a properly constrained design, this is equivalent to Range = $V_\infty t_c$; using Eq. (12) helps relate important design parameters (such as those that affect weight) directly to the objective rather than relying solely on constraints to direct the optimizer to a favorable design.

H. Optimization Framework

Optimizations in this work use Sparse Nonlinear OPTimizer (SNOPT) [51], an SQP algorithm for gradient-based, constrained optimization. Providing the optimizer with exact derivatives is ideal to preserve accuracy and reduce computational cost. All models in this work have been written to be smooth and use types compatible with AD. Derivatives in our framework are evaluated using forward-mode AD [52].

The optimization framework for the studies in this work is depicted in Fig. 5, while Table 4 lists the objective, design variables, and constraints for the optimizations. Design variables include blade geometry (radius, chord and twist distributions), structural parameters (airfoil thickness-to-chord ratio and ply tape thickness distributions), power train parameters (motor K_V and number of battery cells in parallel and in series), and other operating parameters (freestream velocity in cruise, collective pitch in cruise and the OEI case, and rotational velocity for each operating condition). Chord, twist, and thickness distributions were modeled with Akima splines [53]. The number of battery cells in series and parallel are integer quantities, but for compatibility with gradient-based optimization we include them as continuous design variables in the battery equations. After optimizing, we round these to the nearest integer, then re-optimize all remaining design variables (i.e., dynamic rounding). While battery pack design requires additional considerations, which would likely require adjusting the total number of cells, this level of modeling captures the tradeoffs in battery mass with voltage and current requirements.

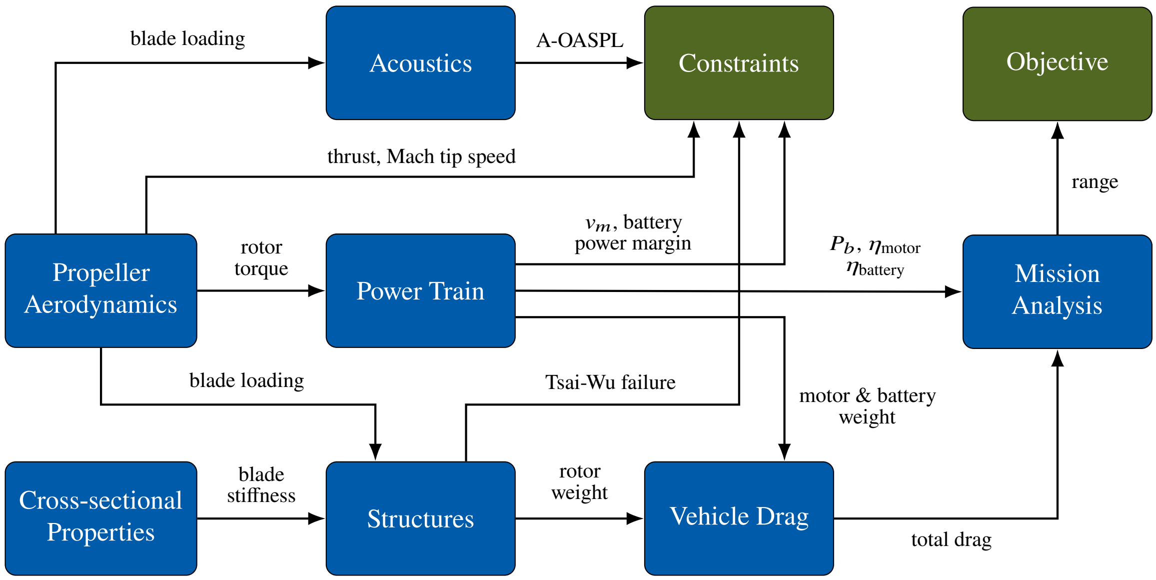

Fig. 5 Simplified layout of the optimization framework. Blue boxes denote models of the system and green boxes denote outputs of the system.

Constraints ensure sufficient thrust (equal to total aircraft weight in the hover and OEI operating points and total drag in the cruise operating point) and ensure no material failure at any blade section in any operating condition. With these constraints, we apply additional safety factors, including a 10% markup in thrust and a material strength markdown of 50%. There are additional constraints on the battery power margin to ensure the rotor is not requiring more power than the battery can supply as well as ensuring the motor voltage is lower than the battery voltage. For the aero-structural optimizations, the Mach tip speed is constrained to a maximum of 0.5 for normal operating conditions and 0.7 for the OEI case. (In this scenario, noise is not an issue and the driving constraints ensure the aircraft can still support its own weight; however, enforcing a limit of 0.7 does avoid aerodynamic inefficiencies associated with supersonic flow.) The aero-structural-acoustic optimizations in this work also include an acoustic constraint on the total A-weighted OASPL which replaces the tip speed constraint of 0.5 (though we maintain a tip speed constrain of 0.7 to avoid compressibility effects).

Table 4 Optimization problem, including the quantity and lower and upper bounds for all design variables and constraints.

	Variable	Lower bound	Upper bound	Quantity
maximize	range			
with respect to	propeller radius	0.3 m	2.0 m	1
	blade chord	2 cm	30 cm	5
	blade twist	-5°	90°	5
	blade airfoil t/c ratio	0.06	0.24	5
	blade tape ply thickness	1 mm	50 mm	5
	collective pitch: cruise	0°	45°	1
	collective pitch: OEI	-45°	0°	1
	cruise speed	35 m/s	120 m/s	1
	propeller rotational speed	100 RPM	5000 RPM	3
	battery cells in series	1	1000	1
	battery cells in parallel	1	1000	1
	motor K_V	10 RPM/V	1000 RPM/V	1
	total design variables			30
subject to	thrust	vehicle weight/drag		3
	Mach tip speed: hover/cruise		0.5/0.7	2
	Mach tip speed: OEI		0.7	1
	Tsai Wu failure		1.0	9122
	battery power margin	0.0		3
	motor voltage		battery voltage	3
	A-weighted OASPL		offset from baseline (dBA)	1
	total constraints			9135

III. Results and Discussion

Using the methods described in Section II and Table 4, we present results from two approaches to optimizing tilt-rotor electric propulsion systems using gradient-based optimization. The first, outlined in Section III.A, is a primarily aerostructural optimization. Models for battery and motor performance are also included, but acoustic performance is limited to a mere constraint on the blade tip speed. The second approach (Section III.B) mirrors the first while modeling tonal and broadband noise of the rotors in the system with an associated constraint on A-OASPL. After discussing these results, we compare optimal designs of the two problems.

A. Aerostructural optimization

Results for the aerostructural optimization are shown in Fig. 6, including distributions for blade chord, twist, airfoil thickness-to-chord ratio, and unidirectional ply thickness, as well as the optimal cross-sectional layup at the blade root colored by the resulting Tsai Wu failure criterion at each element. Each curve is overlayed with the initial starting point for the optimization in gray. The initial design has a range of 61.3 km and an endurance of 13.6 min while the optimized design has range of 207.8 km and a cruise endurance of 60.8 min.

The chord planform follows a typical propeller chord design with a higher root chord (where the stresses are highest in the blade) and a tapered chord as it nears the tip. Twist is high at the root and gradually decreases toward the tip. The

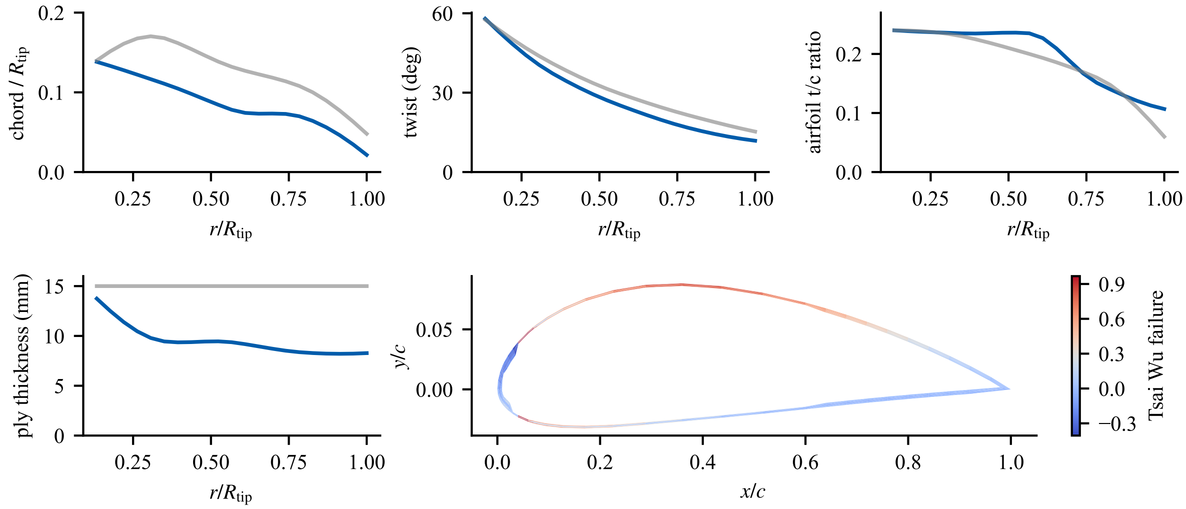

Fig. 6 Optimized blade planform, twist, t/c ratio, and tape ply thickness distributions (blue) overlayed with the initial design (gray). Also shown is the Tsai-Wu failure at the blade root.

airfoil thickness-to-chord ratio and ply thickness distributions are relatively high on the inboard side of the blade and get thinner toward the tip, though neither approaches the lower bound allowed by the optimizer. (Airfoil thickness is at or close to its upper bound on the inboard side of the blade.) Higher inboard thicknesses strengthen the blade and lower outboard thicknesses reduce rotor weight.

Observing the Tsai Wu failure profile for the root cross-sectional mesh in Fig. 6, much of the top-surface laminate is at or close to failure while the rest of the mesh elements have inactive failure constraints. (Note that a Tsai Wu value of 1.0 indicates failure, after having already applied a safety factor to material properties.) Table 5 lists other optimal parameter values and performance metrics. Note that the thrust coefficient is defined differently for hover ($C_{T,\text{hover}} = T/(\rho\pi\Omega^2 R_{\text{tip}}^3)$) and cruise ($C_{T,\text{cruise}} = 4\pi^2 T/(\rho\Omega^2 R_{\text{tip}}^4)$), following standard helicopter and propeller conventions, respectively.

Table 5 Optimized design parameters and outputs.

Design Parameter	Optimized Value
R_{tip}	1.05 m
cruise speed	57.0 m/s
Ω_{hover}	1557.1 RPM
Ω_{cruise}	1052.5 RPM
Ω_{OEI}	2146.6 RPM
collective pitch (cruise)	11.3 deg
collective pitch (OEI)	−11.4 deg
K_V	10 RPM/V
battery cells in series	298
battery cells in parallel	174

Output	Optimized Value
range	207.8 km
cruise endurance	60.8 min
hover disk loading	19.3 lbf/ft^2
hover power loading	6.23 lbf/hp
hover figure of merit	0.721
cruise η_{prop}	79.4%
$C_{T,\text{hover}}$	0.0256
$C_{T,\text{cruise}}$	0.0348
battery weight fraction	57.3%
total weight	7855.3 lbf

Fig. 7 (a) shows the progression of state of charge through the course of the mission, including the takeoff, cruise, landing, and reserve segments and (b) shows the amount of time and energy the hover and cruise mission segments use. Hover refers to both takeoff and landing, and cruise includes the reserve segment in addition to the main cruise segment. Despite taking up just 6% of the total flight time, the hover segments use approximately 35% of the available energy of the system. Because cruise takes up the majority of the mission time, improvements to cruise performance can have significant effects on range. However, the disproportionate amount of energy spent in the hover mission segments highlights the benefits that can come from increasing hover performance (e.g., using less power in hover gives the cruise stage more energy to fly farther). Optimization is key to navigating this tradeoff.

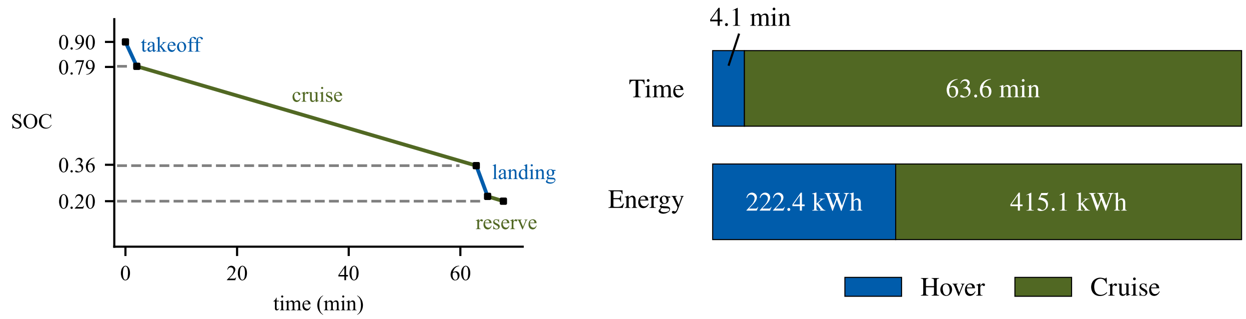

(a) State of charge vs time.

(b) Time and energy used in the hover and cruise mission segments.

Fig. 7 Mission performance of the optimized design.

In addition to analyzing the optimal design, it's important to understand the design space and explore unique tradeoffs and sensitivities of the design to specific parameters. We analyzed such sensitivities for the following parameters: vehicle weight (payload plus empty weight)), battery specific energy, and blade tip speed. We ran these studies by adjusting the parameter of interest and then reoptimizing the propulsion system at every iteration from the same starting point. The following sections will look into each of these sensitivity studies in more detail.

1. Sensitivity to structural weight

Our first sensitivity study shows the effect of changing the vehicle weight of the aircraft. This parameter consists of the empty aircraft weight plus payload weight; it neglects battery, motor, and rotor weight, since these cannot be predetermined before an optimization. We swept this parameter from 1500–4000 lbs, reoptimizing the design with all other parameters equal. In Fig. 8, we show the effect of this sweep on rotational velocity in hover, blade radius, hover and cruise efficiencies, battery mass fraction, battery mass, and range.

As payload/empty weight increases, the rotors need to supply more thrust. To do this, the optimizer increases blade radius (see Fig. 8(b)) and chord along the blade (along with slight increases in twist and airfoil thickness). To satisfy the blade tip speed constraint, it pairs these changes with a reduction in rotational velocity (Fig. 8(a)).

How does this parameter affect hover and cruise performance? We can compare the rotor effectiveness in hover and cruise by comparing the change in hover power loading and cruise rotor propulsive efficiency, η_{prop}, shown in Fig. 8(c) and (d), respectively. We use power loading to measure hover rotor efficiency to easily compare to other rotor designs of varying disk loading. In this parameter sweep, we observe that the optimizer prioritizes hover performance as vehicle weight increases. Over this sweep, cruise propulsive efficiency decreased from 84% to 76.5%. Power loading in hover remained relatively unchanged for the first few optimal designs and then significantly increased as the vehicle weight increased. With a 25% increase in vehicle weight from 3000–4000 lbs, hover power loading increased by 20.8% from 6.0 to 7.25 lbf/hp. This increase in power loading is coupled with a decrease in disk loading. This is in contrast to standard helicopters, where a heavier vehicle typically leads to higher disk loading and lower power loading [54]. As opposed to helicopters, which are already at or close to their limit for disk area due to compressibility and noise constraints, the optimizer in this system chooses to lower disk loading by increasing disk area more than the increase in required thrust. In this parameter sweep and those that follow, we observe a recurring pattern: as the system requirements become more restrictive (e.g., more weight), the optimizer gives priority to improving rotor efficiency in hover.

We also observe changes to the amount of battery energy the optimizer chooses to include in the system (see Fig. 8(e) and (f)). As more thrust is required, the optimizer could add more battery cells—this would supply more energy and power, but also come with a weight penalty which requires even more energy and power. Or the optimizer could remove battery cells, making the thrust demands more manageable to improve efficiency. In this case, we observe that as vehicle weight increases, battery mass fraction of the system consistently decreases. Over the range of this parameter sweep, the battery mass fraction decreases from 72% to 51%. However, the decision of whether to add or remove battery cells is not straightforward. Up until a vehicle weight of 3000 lbs, the optimizer adds battery cells to the system. As the vehicle

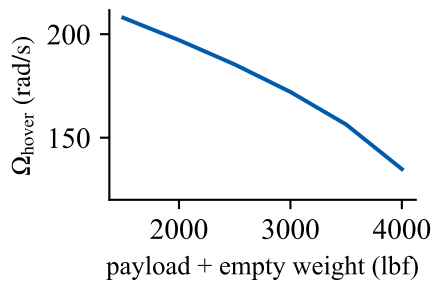

(a) Rotational speed in hover

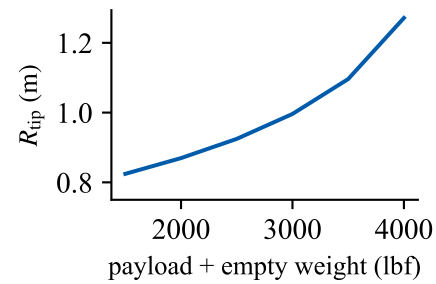

(b) Blade radius

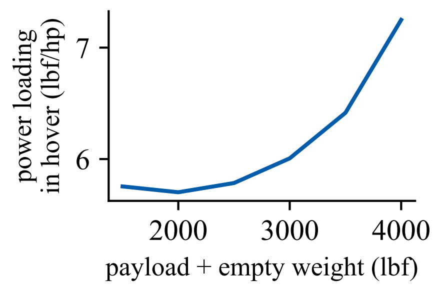

(c) Power loading in hover

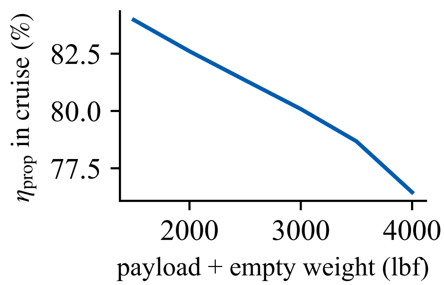

(d) Propulsive efficiency in cruise

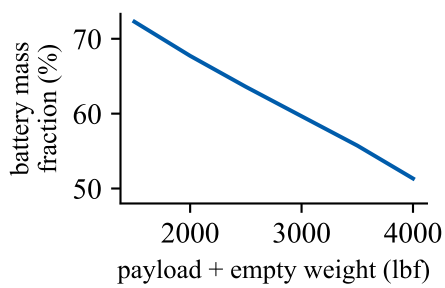

(e) Battery mass fraction

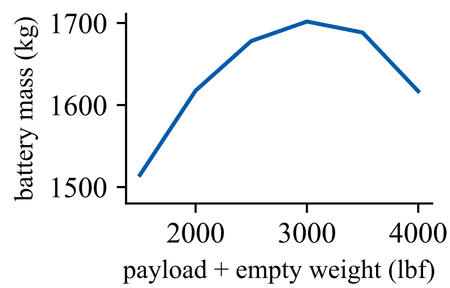

(f) Battery mass

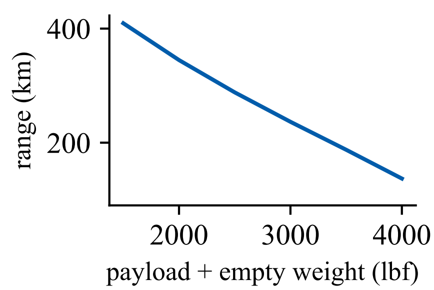

(g) Range

Fig. 8 Design sensitivities to the payload plus empty weight of the aircraft from 1500–4000 lbf.

weight continues to increase, it removes battery cells from the system. To maximize range, there appears to be a pivotal design point where adding more available energy to the system is not worth the additional weight penalty; the battery can no longer support its own weight with additional cells.

Overall, the payload and empty weight parameters have a significant effect on range (Fig. 8(g)). We observe a decrease in range of about 100 km for every increase in payload/empty weight of 1000 lbf. This tradeoff is slightly more pronounced at the lower portion of the sweep; increasing weight from 1500–2500 lbf decreases range by 122 km.

2. Sensitivity to battery specific energy

Fig. 9 shows sensitivities with respect to battery specific energy, ranging from 300 Wh/kg (current battery technology) to 500 Wh/kg (reflecting projected long-term advances in battery technology [47]) at the cell level. Batteries with higher energy densities can have the same available energy for a lower weight penalty.

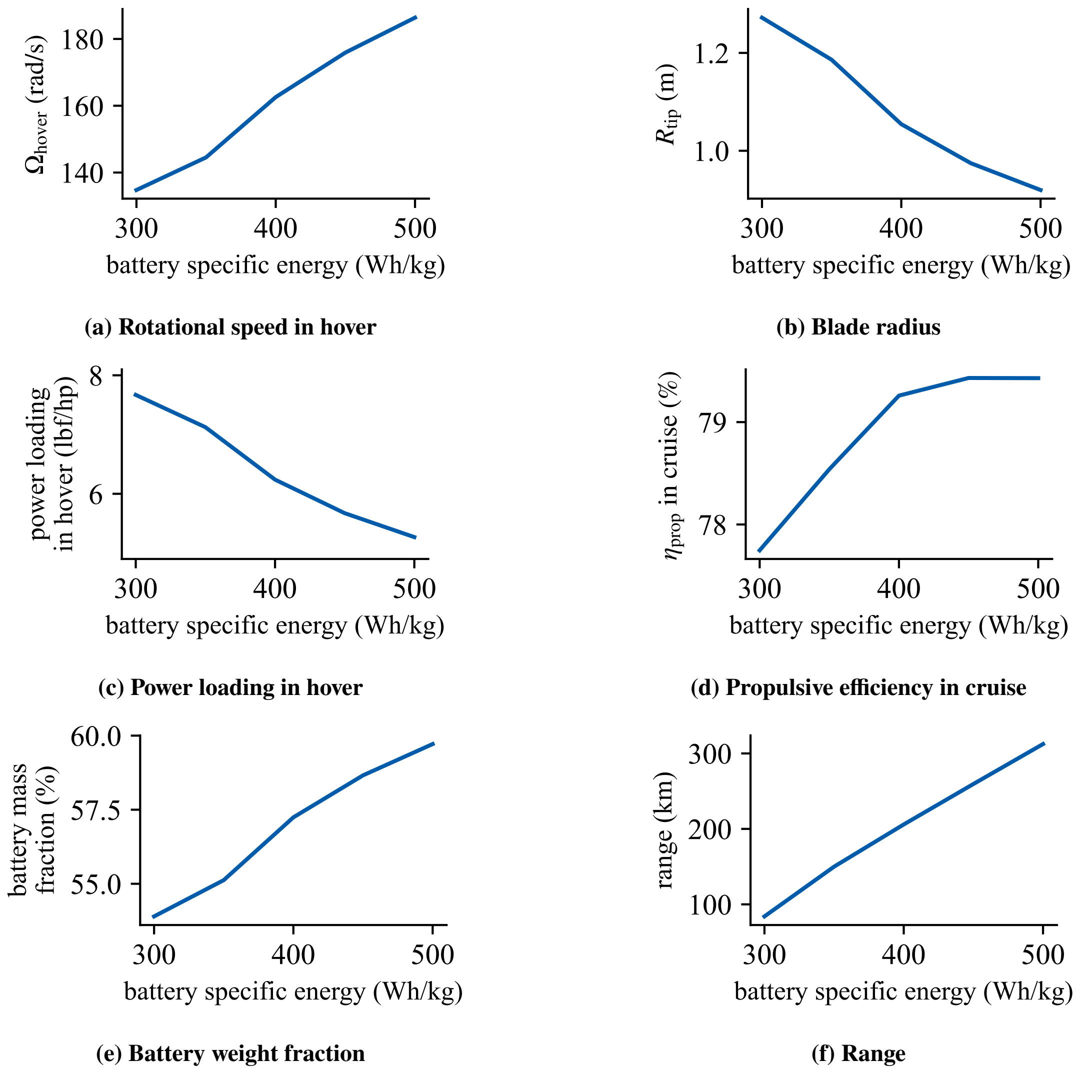

(a) Rotational speed in hover

(b) Blade radius

(c) Power loading in hover

(d) Propulsive efficiency in cruise

(e) Battery weight fraction

(f) Range

Fig. 9 Design sensitivities to the battery energy density ranging from 300 to 500 Wh/kg (at the cell level).

As we increase the specific energy, the optimizer chooses to add more battery cells to the system to optimize range (see the increase in battery mass fraction in Fig. 9(e)), rather than simply flying farther with the same battery mass or removing battery cells to save weight. In the previous section, we observed there was a point where the optimizer removed battery cells because the battery could not support the weight of additional cells. As we increase the battery specific energy, the critical point where the battery can no longer support its own weight has been delayed; we don't observe that behavior in this studied range of values.

To account for the increased weight, Ω_{hover} increases with an accompanying decrease in blade radius to satisfy the tip speed constraint (see Fig. 8(a) and (b)). This behavior is in direct contrast to the previous sensitivity study with payload/empty weight, where the optimizer met an increasing thrust demand with a larger blade radius and lower rotational speed in hover. While the blade planform and twist profiles remain relatively unchanged, the change in radius is still significant. Thus, as battery technology improves, rotor blade design optimization will remain necessary to ensure range remains optimal; rotor blade designs that are optimal for current battery parameters will not be optimal when those parameters change. However, those ensuing optimizations can potentially avoid complexity by reusing the same normalized chord and twist distributions and only changing radius, removing several design variables from the problem.

In Fig. 8(c) and (d), we observe that as battery technology improves, power loading in hover decreases and cruise propulsive efficiency slightly increases. The optimizer maximized range with an improvement of about 1.7% in η_{prop} despite the tradeoff of a decrease in hover power loading of 2.4 lbf/hp, or 31%. This behavior follows the same pattern as the weight sensitivity study—with more restrictions on the system (e.g., less battery specific energy) the optimizer favors hover efficiency over cruise efficiency.

These changes result in significant effects on range (Fig. 8(f)); for every 50 Wh/kg of additional battery specific energy, the system gains approximately 57 km of range. These results highlight the importance of optimization in making design decisions. With improved battery performance, range is not maximized by simply flying farther with the same system.

3. Sensitivity to blade Mach tip speed constraint

We performed a similar analysis of sensitivities to the Mach speed restriction at the blade tip from 0.35 to 0.6. A looser restriction on the Mach tip speed, (i.e., raising the upper bound), decreases blade radius while increasing Ω_{hover} (see Fig. 10(a) and (b)). These effects are significant: increasing the Mach tip speed from 0.35 to 0.6 increases optimal Ω_{hover} by 123% and decreases optimal radius by 26%. These changes are accompanied by a decrease in chord and twist along the blade.

When we increase the tip speed constraint (which is an active constraint in hover and an inactive constraint in cruise), we observe that the optimizer prioritizes cruise rotor performance. Increasing this upper limit on blade tip speed from 0.35 to 0.6 resulted in a decrease in hover efficiency from 8.4 to 5.5 lbf/hp—a 35% change (Fig. 10(c)), and an increase in cruise efficiency of 8.8% (from 72.8% to 81.6%—see Fig. 10(d)). This has a similar behavior to the vehicle weight sensitivity study; as the constraint on the system becomes more restrictive (a lower Mach tip speed, in this instance), hover performance is prioritized at the expense of cruise performance. This follows naturally from the fact that system constraints are typically active in the hover operating mode where there are larger thrust and power requirements on the system. Allowing the optimizer to increase blade tip speed gives it flexibility to increase cruise efficiency enough to make up for the added power usage in hover.

This constraint has a large effect on range (Fig. 10(e)); increasing blade Mach tip speed from 0.35 to 0.45 leads to approximately 100 km of additional range, or a 136% increase. There is, however, a trend of diminishing returns; increasing the Mach tip speed has a larger effect at lower tip speeds. For instance, a Mach tip speed increase from 0.5 to 0.6 increases range by only 49 km, or 24%. One main drawback of high tip speeds is, of course, extreme levels of noise. While not included as a constraint in these optimizations, we can analyze the A-OASPL of each design in postprocessing. We find that noise levels increase substantially with tip speed (Fig. 10(f)). Increasing the constraint from 0.5 to 0.6 leads to an increase in A-OASPL of over 27 dBA. While it is difficult to convert blade tip speed to specific A-OAPSL values, this does show the effectiveness of using a tip speed constraint as a surrogate model for noise. In Section III.B, we compare this method with that of modeling tonal and broadband noise directly to optimize rotor designs.

B. Aero-structural-acoustic optimization

Thus far, all of our optimization studies used a Mach tip speed constraint to limit noise of the propulsion system. While the blade tip speed is directly correlated with noise, this model neglects important acoustic sources, such as those from blade geometry, loading, and multiple blades and rotors, while also being unable to weight the noise output according to specific frequencies. We implement methods described in Section II.D to add an additional constraint to the system for A-OASPL. This effectively replaces the previously active Mach tip speed constraint of 0.5, though we maintain a tip speed constraint of Mach 0.7 to avoid transonic flow regimes (this was an inactive constraint for all cases). The new acoustic constraint restricts the A-OASPL at the observer described in Section II.D. A baseline optimal design without an A-OASPL constraint (and a blade tip speed constrained to Mach 0.7) produces about 100 dBA of noise. We ran a series of aero-structural-acoustic optimizations with an A-OASPL constraint that started at this baseline value of 100 dBA and incrementally reduced the constraint until 55 dBA, after which the optimizations failed to converge.

We can visualize the range sensitivity to this constraint value as a Pareto front, as shown in Fig. 11. At relatively high A-OASPL constraint values, the range penalty for reducing noise by 5 dBA can be from 6.6-9.6 km (i.e. about a 2-3% penalty). However, this cost increases sharply at constraint values below 70 dBA. From an A-OASPL constraint of 70 to 65 dBA, range decreases by 11.7 km (5.6%); from 65 to 60 dBA, range decreases by 17.4 km (8.8%); and from 60 to 55 dBA, range decreases by 31 km (17.25%). The Pareto front offers insight into high-level design decisions to

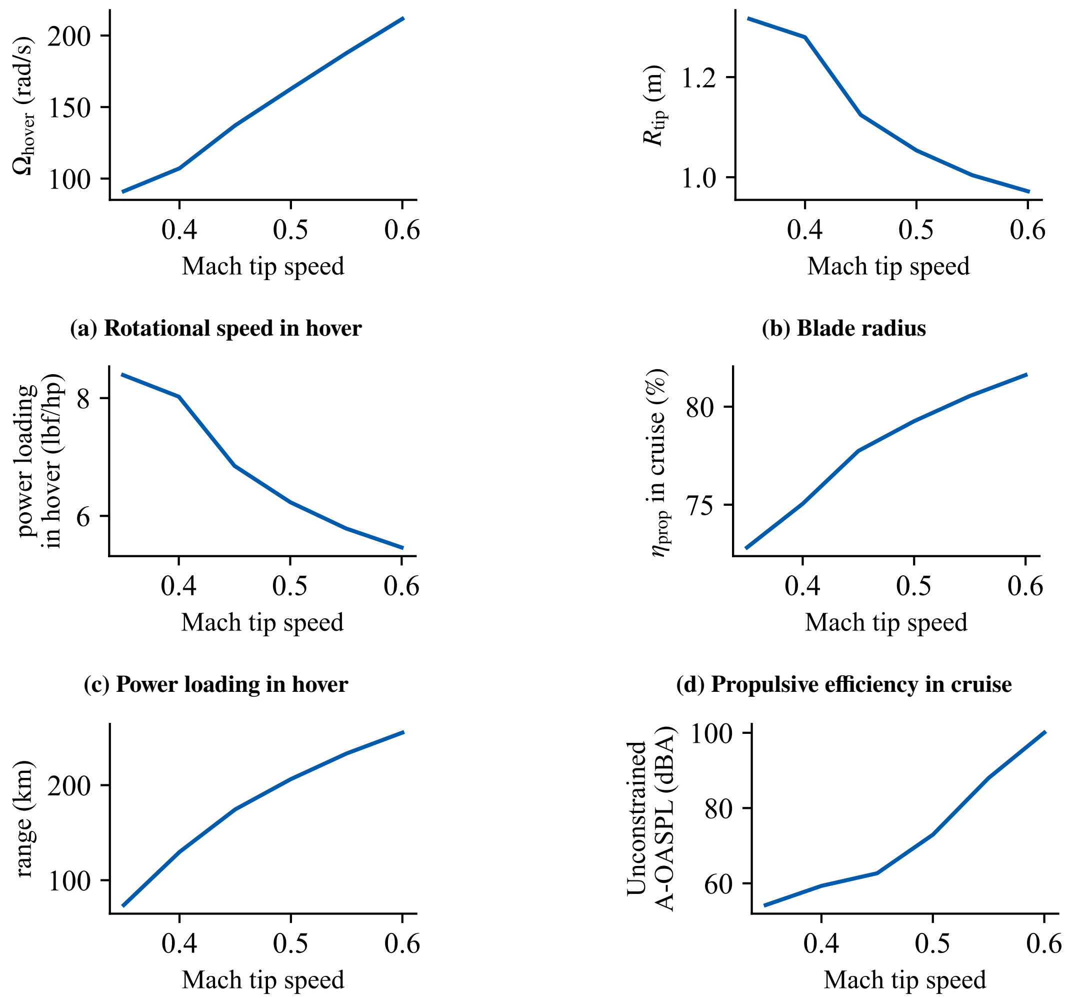

(a) Rotational speed in hover

(b) Blade radius

(c) Power loading in hover

(d) Propulsive efficiency in cruise

(e) Range

(f) Unconstrained A-OASPL

Fig. 10 Design sensitivity to Mach tip speed constraint ranging from 0.35 to 0.6.

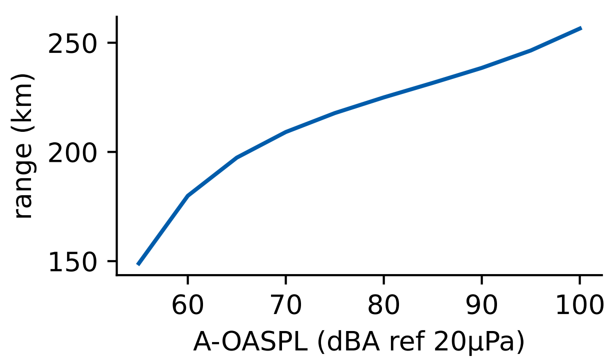

Fig. 11 Pareto front comparing A-OASPL constraint to optimal range.

know how much range will be sacrificed to obtain a specific noise outcome—or alternatively, how much louder the system will be if extra range is desired. In this case, there is not a point in this tradeoff where a lot of noise can be reduced for little sacrificed range; however, there are designs where a little noise reduction can lead to large sacrifices in range. Quiet tilt-rotor systems do not come without a cost.

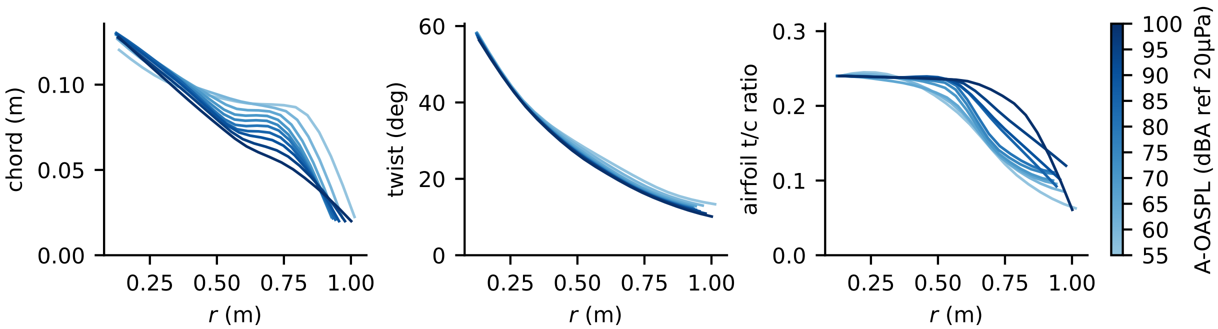

(a) Blade chord, twist, and airfoil t/c distributions

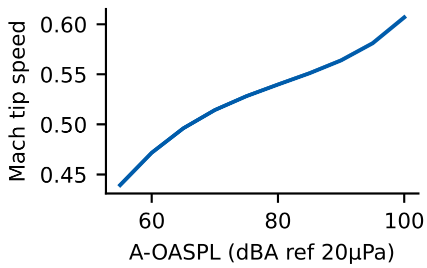

(b) Mach tip speed

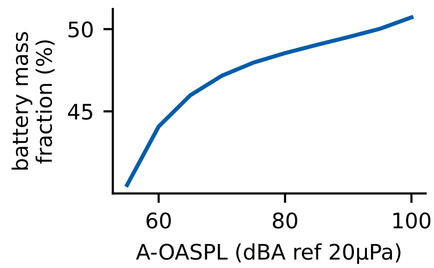

(c) Battery mass fraction

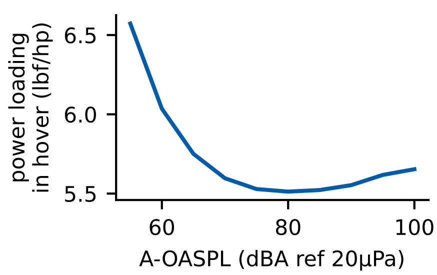

(d) Power loading in hover

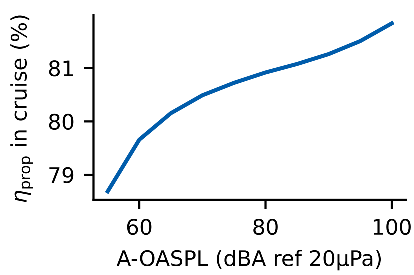

(e) Propulsive efficiency in cruise

Fig. 12 Design sensitivity to the A-OASPL constraint value, ranging from 100 to 55 dBA.

Fig. 12 gives additional insight into how the optimizer is choosing to reduce noise by looking at sensitivities for blade geometry, operating parameters, and efficiency metrics. In general, the optimizer increases chord and twist when needing to reduce additional noise, especially on the outboard portion of the blade. (Note that a reduction in noise corresponds to lighter-colored curves in Fig. 12(a).) It also significantly decreases airfoil thickness along most of the blade. It reduces its tip speed (Fig. 12(b)) and takes on fewer battery cells (Fig. 12(c)). However, the blade radius trend is not as simple to track. At first, the optimizer reduces the radius, but with A-OASPL constraint values less than 75 dBA, it begins to increase the radius (see Fig. 12(a)). The lower rotational speed (and corresponding tip speed) is certainly a big factor the optimizer is using to reduce noise.

As the A-OASPL gets further restricted, the optimizer does not significantly change the hover power loading or cruise propulsive efficiency until around the 75 dBA mark, after which it increases hover power loading and decreases cruise efficiency at a higher rate (see Fig. 12(d) and (e)). This highlights an interesting conclusion: at more restrictive noise constraints, optimal tilt-rotor designs with less noise output are correlated with higher hover efficiency performance. In this case, aerodynamic efficiency in hover was not in direct competition with a quieter rotor; however, there was still the obvious cost of range, the mission objective.

We can make additional comparisons to optimal designs with and without the A-OASPL constraint to determine the effectiveness of using a tip speed constraint over higher-fidelity acoustic models. To compare like designs, we performed an acoustics analysis on the baseline optimal design from Section III.A. This design has a maximum Mach tip speed of 0.5 during the optimization and produces an A-OASPL of 72.8 dBA. We ran an additional optimization with the modified Mach tip speed constraint of 0.7 and an A-OASPL constraint matching that of 72.8 dBA. Comparing these two optimal designs ensures a comparison between designs with the same A-weighted noise footprint; the main difference is that in the first case, the optimizer could not have a tip speed higher than 0.5 (this was an active constraint) and A-OASPL was unconstrained; in the second case, Mach tip speed was constrained to a maximum value of 0.7 to avoid compressibility effects (an inactive constraint) while A-OASPL was constrained. However, both have the same A-weighted total noise output.

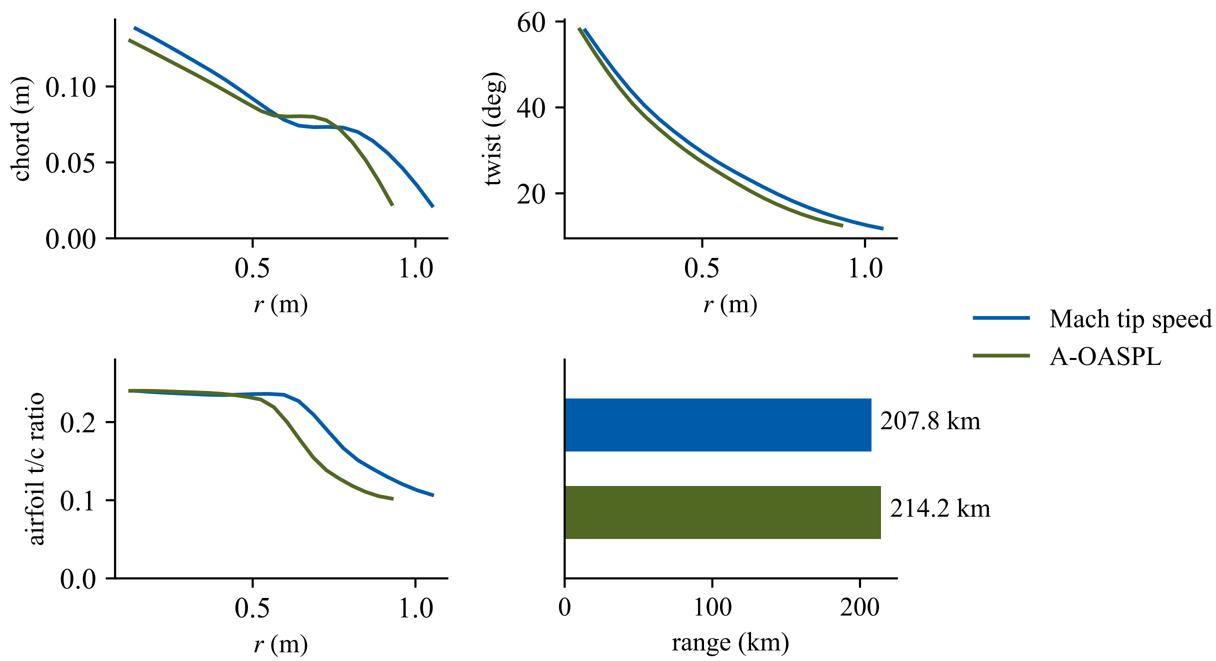

Fig. 13 Comparing optimized designs with constraints for Mach tip speed (blue) and A-OASPL (green).

By constraining A-OASPL from tonal and broadband noise models, we achieve an increase in range of 3.1% compared to using a comparable Mach tip speed constraint. Without the tip speed restriction of Mach 0.5, the optimizer chooses to go slightly past that to 0.52. It does this by reducing the blade radius and increasing Ω_{hover}. This results in a higher disk loading (28.1%) and a reduction in power loading (10.9%). Thus, the optimizer is making the hover propeller less efficient compared to the optimal design with only a tip speed constraint. This is offset by an improvement in cruise performance from increased propulsive and motor efficiencies, lower battery and rotor weights, and increased collective pitch, rotational velocity and freestream velocity in cruise. As shown in Fig. 13, there are also subtle differences in blade chord, twist, and airfoil thickness profiles.

These optimizations show that a Mach tip speed constraint can be an adequate surrogate for modeling rotor noise in design optimization. It is more computationally efficient and results in an optimal design close to that obtained with the framework that includes models for tonal and broadband noise. However, a tip speed constraint has limitations. A tip speed constraint cannot easily be converted to a concrete OASPL value, which is important when a specific noise outcome is desired. Thus, a tip speed constraint can easily become an arbitrary cutoff value chosen by the user that merely restricts blade radius and rotational speed and cannot account for changes to blade geometry and other operating parameters that could improve noise output. In this case, those additional changes resulted in an improved range of 6.4 km, or 3.1%.

IV. Conclusion

In this paper, we perform multidisciplinary gradient-based design optimization on a tilt-rotor electric propulsion system with a framework that uses forward-mode algorithmic differentiation and a multi-operating point, mission-focused objective. This approach includes models for propeller performance (blade element momentum theory), blade structures (geometrically exact beam theory), acoustics (Mach tip speed as well as tonal and broadband noise models), and low-fidleity physics-based models for vehicle drag and motor and battery performance. We also implement a B-spline fit of precomputed airfoil polars for a unique family of airfoils generated based on the MH-114 airfoil, only varying by max thickness.

This optimization framework allows for effective parameter design sensitivity studies where we highlight parameters that have a significant effect on range for a conceptual tilt-rotor eVTOL aircraft. We also run a sensitivity study on the constraint imposed on the A-weighted overall sound pressure level (A-OASPL) and generate a Pareto front for range and acoustic output.

We find that this optimization framework is successful in navigating the complex tradeoffs between hover and cruise performance for a tilt-rotor system. For instance, using a lighter aircraft/payload, a less-restrictive tip speed, and higher battery specific energies all cause the optimizer to decrease hover efficiency and increase cruise efficiency to optimize range. For the same total A-OASPL of the system, constraining A-OASPL from tonal and broadband noise models improved range by 3.1% over using a Mach tip speed constraint as a surrogate acoustics model. Optimization studies that merely use a blade tip speed constraint to constrain acoustic output are placing an arbitrary limit on the optimizer and missing out on potential improvements to their objective.

Additionally, we observe that airfoil performance has a large effect on the ability of the optimizer to converge for these problems, highlighting the need for future work to incorporate airfoil design into the optimization framework rather than using a fit made from precomputed polars. Future work can also improve model fidelity (e.g., incorporating wing design and wing-propeller aerodynamic interactions), as well as comparing with other vehicle configurations, such as the lift+cruise design which would need separately optimized hover and cruise rotors.

V. Acknowledgements

The material presented in this paper is based upon work supported by NASA under award No. 80NSSC21M0070.

References

[1] Johnson, W., and Silva, C., "Observations from Exploration of VTOL Urban Air Mobility Designs," *7th Asian/Australian Rotorcraft Forum*, Vertical Flight Society, Jeju Island, Korea, 2018.

[2] Johnson, W., and Silva, C., "NASA concept vehicles and the engineering of advanced air mobility aircraft," *The Aeronautical Journal*, Vol. 126, No. 1295, 2022, pp. 59–91. doi:10.1017/aer.2021.92.

[3] Kadhiresan, A. R., and Duffy, M. J., "Conceptual Design and Mission Analysis for eVTOL Urban Air Mobility Flight Vehicle Configurations," *AIAA Aviation 2019 Forum*, 2019. doi:10.2514/6.2019-2873.

[4] Whiteside, S. K., Pollard, B. P., Antcliff, K. R., Zawodny, N. S., Fei, X., Silva, C., and Medina, G. L., "Design of a Tiltwing Concept Vehicle for Urban Air Mobility," Tech. Rep. NASA TM–20210017971, NASA Langley Research Center, June 2021.

[5] Moore, M., "NASA Puffin Electric Tailsitter VTOL Concept," *10th AIAA Aviation Technology, Integration, and Operations (ATIO) Conference*, 2010, p. 9345. doi:10.2514/6.2010-9345.

[6] Bacchini, A., and Cestino, E., "Electric VTOL Configurations Comparison," *Aerospace*, Vol. 6, No. 3, 2019. doi:10.3390/aerospace6030026.

[7] Whitt, J., and Gandhi, F., "Optimal Operation of Rotor-Wing Assemblies on eVTOL Aircraft," *Proceedings of the Vertical Flight Society 79th Annual Forum*, West Palm Beach, FL, 2023. doi:10.4050/F-0079-2023-18008.

[8] Beals, N., "Aerodynamic Optimization of a Small UAS Rotor for a Mission with Hover and Forward-Flight Segments," *American Helicopter Society 74th Annual Forum*, 2018. doi:10.4050/F-0074-2018-12716.

[9] Droandi, G., and Gibertini, G., "Aerodynamic shape optimisation of a proprotor and its validation by means of CFD and experiments," *The Aeronautical Journal*, Vol. 119, No. 1220, 2015, pp. 1223–1251. doi:10.1017/S0001924000011222.

[10] Jimenez-Garcia, A., Biava, M., Barakos, G., Baverstock, K., Gates, S., and Mullen, P., "Tiltrotor CFD Part II-aerodynamic optimisation of tiltrotor blades," *The Aeronautical Journal*, Vol. 121, No. 1239, 2017, pp. 611–636. doi:10.1017/aer.2017.21.

[11] Hendricks, E. S., Falck, R. D., Gray, J. S., Aretskin-Hariton, E., Ingraham, D., Chapman, J. W., Schnulo, S. L., Chin, J., Jasa, J. P., and Bergeson, J. D., "Multidisciplinary Optimization of a Turboelectric Tiltwing Urban Air Mobility Aircraft," *AIAA Aviation 2019 Forum*, Dallas, TX, 2019, p. 3551. doi:10.2514/6.2019-3551.

[12] Hendricks, E. S., Aretskin-Hariton, E., Ingraham, D., Gray, J. S., Schnulo, S. L., Chin, J., Falck, R., and Hall, D., "Multidisciplinary Optimization of an Electric Quadrotor Urban Air Mobility Aircraft," *AIAA AVIATION 2020 FORUM*, 2020. doi:10.2514/6.2020-3176.

[13] Hoyos, J. D., Jímenez, J. H., and Alvarado, P., "Improvement of Electric Aircraft Endurance through Propeller Optimization via BEM-CFD Methodology," *Journal of Physics: Conference Series*, Vol. 1733, IOP Publishing, 2021. doi:10.1088/1742-6596/1733/1/012011.

[14] Mian, H. H., Wang, G., Zhou, H., and Wu, X., "Optimization of thin electric propeller using physics-based surrogate model with space mapping," *Aerospace Science and Technology*, Vol. 111, 2021, p. 106563. doi:10.1016/j.ast.2021.106563.

[15] Xia, X., Ma, D., Zhang, L., Liu, X., and Cong, K., "Blade Shape Optimization and Analysis of a Propeller for VTOL Based on an Inverse Method," *Applied Sciences*, Vol. 12, No. 7, 2022, p. 3694. doi:10.3390/app12073694.

[16] Zawodny, N. S., Pettingill, N. A., Lopes, L. V., and Ingraham, D. J., "Experimental Validation of an Acoustically and Aerodynamically Optimized UAM Proprotor Part 1: Test Setup and Results," Tech. Rep. 20220015637, NASA Langley Research Center, 2023.

[17] Gur, O., Silver, J., Dítě, R., and Sundhar, R., "Optimized Performance and Acoustic Design for Hover-Propeller," *AIAA Aviation 2021 Forum*, 2021. doi:10.2514/6.2021-2222.

[18] Ingraham, D., Gray, J. S., and Lopes, L. V., "Gradient-Based Propeller Optimization with Acoustic Constraints," *AIAA Scitech 2019 Forum*, 2019. doi:10.2514/6.2019-1219.

[19] Moore, K., and Ning, A., "Takeoff and Performance Tradeoffs of Retrofit Distributed Electric Propulsion for Urban Transport," *Journal of Aircraft*, Vol. 56, No. 5, 2019, pp. 1880–1892. doi:10.2514/1.C035321.

[20] Hwang, J., and Ning, A., "Large-scale multidisciplinary optimization of an electric aircraft for on-demand mobility," *2018 AIAA Structures, Structural Dynamics, and Materials Conference*, Kissimmee, FL, 2018. doi:10.2514/6.2018-1384.

[21] Shahjahan, S., Gong, A., Moore, A., and Verstraete, D., "Optimisation of proprotors for tilt-wing eVTOL aircraft," *Aerospace Science and Technology*, Vol. 144, 2024, p. 108835. doi:10.1016/j.ast.2023.108835.

[22] Clarke, M. A., Erhard, R. M., Smart, J. T., and Alonso, J., "Aerodynamic Optimization of Wing-Mounted Propeller Configurations for Distributed Electric Propulsion Architectures," *AIAA AVIATION 2021 FORUM*, 2021. doi:10.2514/6.2021-2471.

[23] Ning, A., "A Simple Solution Method for the Blade Element Momentum Equations with Guaranteed Convergence," *Wind Energy*, Vol. 17, No. 9, 2014, pp. 1327–1345. doi:10.1002/we.1636.

[24] Ning, A., "Using Blade Element Momentum Methods with Gradient-Based Design Optimization," *Structural and Multidisciplinary Optimization*, Vol. 64, No. 2, 2021, pp. 994–1014. doi:10.1007/s00158-021-02883-6.

[25] Ning, A., and McDonnell, T., "Automating Steady and Unsteady Adjoints: Efficiently Utilizing Implicit and Algorithmic Differentiation," 2023. (in review).

[26] Du, Z., and Selig, M., "A 3-D Stall-Delay Model for Horizontal Axis Wind Turbine Performance Prediction," *1998 ASME Wind Energy Symposium*, Reno, NV, 1998. doi:10.2514/6.1998-21.

[27] Eggers Jr, A., Chaney, K., and Digumarthi, R., "An Assessment of Approximate Modeling of Aerodynamic Loads on the UAE Rotor," *Wind Energy Symposium*, Vol. 75944, Reno, NV, 2003, pp. 283–292. doi:10.1115/WIND2003-868.

[28] Viterna, L. A., and Janetzke, D. C., "Theoretical and Experimental Power From Large Horizontal-Axis Wind Turbines," Tech. rep., National Aeronautics and Space Administration, Cleveland, OH (USA). Lewis Research Center, Sep 1982. doi:10.2172/6763041.

[29] Glauert, H., "Airplane Propellers," *Aerodynamic theory*, Springer, 1935, pp. 169–360. doi:10.1007/978-3-642-91487-4_3.

[30] Buhl Jr, M. L., "A New Empirical Relationship between Thrust Coefficient and Induction Factor for the Turbulent Windmill State," Tech. rep., National Renewable Energy Lab.(NREL), Golden, CO (United States), Aug 2005. doi:10.2172/15016819.

[31] Glauert, H., *The Analysis of Experimental Results in the Windmill Brake and Vortex Ring States of an Airscrew*, RM No. 1026, British ARC, 1926.

[32] Kulfan, B. M., "Universal Parametric Geometry Representation Method," *Journal of Aircraft*, Vol. 45, No. 1, 2008, pp. 142–158. doi:10.2514/1.29958.

[33] Drela, M., "XFOIL: An Analysis and Design System for Low Reynolds Number Airfoils," *Low Reynolds Number Aerodynamics: Proceedings of the Conference Notre Dame, Indiana, USA, 5–7 June 1989*, Vol. 54, Springer, Berlin, Heidelberg, 1989, pp. 1–12. doi:10.1007/978-3-642-84010-4_1.

[34] Yu, W., and Blair, M., "GEBT: A general-purpose nonlinear analysis tool for composite beams," *Composite Structures*, Vol. 94, No. 9, 2012, pp. 2677–2689. doi:10.1016/j.compstruct.2012.04.007.

[35] Wang, Q., and Yu, W., "Geometrically nonlinear analysis of composite beams using Wiener-Milenković parameters," *Journal of Renewable and Sustainable Energy*, Vol. 9, No. 3, 2017, p. 033306. doi:10.1063/1.4985091.

[36] Tsai, S. W., and Wu, E. M., "A General Theory of Strength for Anisotropic Materials," *Journal of Composite Materials*, Vol. 5, No. 1, 1971, pp. 58–80. doi:10.1177/002199837100500106.

[37] McDonnell, T., and Ning, A., "GXBeam: A Pure Julia Implementation of Geometrically Exact Beam Theory," *Journal of Open Source Software*, Vol. 7, No. 73, 2022, p. 3997. doi:10.21105/joss.03997.

[38] Ffowcs Williams, J. E., and Hawkings, D. L., "Sound generation by turbulence and surfaces in arbitrary motion," *Philosophical Transactions of the Royal Society of London. Series A, Mathematical and Physical Sciences*, Vol. 264, No. 1151, 1969, pp. 321–342. doi:10.1098/rsta.1969.0031.

[39] Lopes, L. V., "Compact Assumption Applied to Monopole Term of Farassat's Formulations," *Journal of Aircraft*, Vol. 54, No. 5, 2017, pp. 1649–1663. doi:10.2514/1.C034048.

[40] Farassat, F., "Linear Acoustic Formulas for Calculation of Rotating Blade Noise," *AIAA journal*, Vol. 19, No. 9, 1981, pp. 1122–1130. doi:10.2514/3.60051.

[41] Gill, H., and Lee, S., "Development of New Empirical Rotor Broadband Noise Prediction Models for Urban Air Mobility Applications," *AIAA SCITECH 2024 Forum*, Orlando, FL, 2024. doi:10.2514/6.2024-2473.

[42] Brooks, T. F., Pope, D. S., and Marcolini, M. A., "Airfoil Self-Noise and Prediction," Tech. Rep. RP 1218, NASA Langley Research Center, 1989.

[43] Jiang, H., Zhong, S., Wu, H., Zhang, X., Huang, X., Zhou, G., and Chen, B., "Radiation Modes of Propeller Tonal Noise," *Journal of Vibration and Acoustics*, Vol. 144, No. 2, 2021, p. 021009. doi:10.1115/1.4051864.

[44] Bershadsky, D., Haviland, S., and Johnson, E. N., "Electric Multirotor UAV Propulsion System Sizing for Performance Prediction and Design Optimization," *57th AIAA/ASCE/AHS/ASC Structures, Structural Dynamics, and Materials Conference*, San Diego, CA, 2016. doi:10.2514/6.2016-0581.

[45] Clarke, M., and Alonso, J. J., "Lithium–Ion Battery Modeling for Aerospace Applications," *Journal of Aircraft*, Vol. 58, No. 6, 2021, pp. 1323–1335. doi:10.2514/1.C036209.

[46] Zou, Y., Hu, X., Ma, H., and Li, S. E., "Combined State of Charge and State of Health estimation over lithium-ion battery cell cycle lifespan for electric vehicles," *Journal of Power Sources*, Vol. 273, 2015, pp. 793–803. doi:10.1016/j.jpowsour.2014.09.146.

[47] Altouq, S., Fong, C. M., Norman, P. J., and Burt, G., "Technology Maturity Roadmaps of Power System Components for eVTOL Aircraft," Working paper, University of Strathclyde, Glasgow, UK, Sep 2022.

[48] Brent, R. P., "An algorithm with guaranteed convergence for finding a zero of a function," *The Computer Journal*, Vol. 14, No. 4, 1971, pp. 422–425. doi:10.1093/comjnl/14.4.422.

[49] Schlichting, H., and Gersten, K., *Boundary-Layer Theory*, 7^{th} ed., McGraw-Hill Book Company, 1979, pp. 127–149.

[50] "Uber Elevate. Uber Air Vehicle Requirements and Missions," https://s3.amazonaws.com/uber-static/elevate/Summary+Mission+and+Requirements.pdf (Accessed: 21 February 2025), 2018.

[51] Gill, P., Murray, W., and Saunders, M., "SNOPT: An SQP Algorithm for Large-Scale Constrained Optimization," *SIAM Journal of Optimization*, Vol. 47, No. 1, 2005, pp. 99–131. doi:10.1137/S0036144504446096.

[52] Revels, J., Lubin, M., and Papamarkou, T., "Forward-Mode Automatic Differentiation in Julia," *arXiv:1607.07892 [cs.MS]*, 2016. doi:10.48550/arXiv.1607.07892.

[53] Akima, H., "A New Method of Interpolation and Smooth Curve Fitting Based on Local Procedures," *Journal of the ACM*, Vol. 17, No. 4, 1970, pp. 589–602. doi:10.1145/321607.321609.

[54] Leishman, G. J., *Principles of Helicopter Aerodynamics*, 2nd ed., Cambridge University Press, 2006, pp. 280–283.